Effect of heat treatment on functionally graded 304L stainless steel to Inconel 625 fabricated by directed energy deposition

Zhening Yang , Hui Sun , Shun-Li Shang , Zi-Kui Liu , Allison M. Beese

PII: S2589-1529(24)00064-4
DOI: https://doi.org/10.1016/j.mtla.2024.102067
Reference: MTLA 102067

To appear in: *Materialia*

Received date: 6 February 2024
Accepted date: 14 March 2024

Please cite this article as: Zhening Yang , Hui Sun , Shun-Li Shang , Zi-Kui Liu , Allison M. Beese , Effect of heat treatment on functionally graded 304L stainless steel to Inconel 625 fabricated by directed energy deposition, *Materialia* (2024), doi: https://doi.org/10.1016/j.mtla.2024.102067

Effect of heat treatment on functionally graded 304L stainless steel to Inconel 625 fabricated by directed energy deposition

Zhening Yang[a], Hui Sun[a], Shun-Li Shang[a], Zi-Kui Liu[a], Allison M. Beese [a, b*]

[a] Department of Materials Science and Engineering, Pennsylvania State University, University Park, PA 16802, USA

[b] Department of Mechanical Engineering, The Pennsylvania State University, University Park, PA 16802, USA

* Corresponding author: beese@matse.psu.edu

Abstract

Defining appropriate heat treatments for compositionally functionally graded materials (FGMs) is challenging due to varying processing conditions in terminal alloys and gradient regions. Therefore, it is critical to investigate the impact of potential heat treatments on phase transformations and the resulting mechanical properties along the entire compositional path. In the present study, we applied heat treatments at 700 °C, 900 °C, and 1150 °C on a stainless steel 304L (SS304L) to Inconel 625 (IN625) FGM fabricated using directed energy deposition (DED) additive manufacturing (AM). The microstructure and hardness, as a function of layer-wise composition and applied heat treatment, were characterized. The applicability of computational methods previously developed by the team to predict experimentally observed phases by the hybrid Scheil-equilibrium approach was evaluated. This approach improves the accuracy of predicting phases formed after heat treatment compared to equilibrium thermodynamic calculations using the overall layer compositions and provides a simple pathway to assist in designing heat treatment for FGMs.

Keywords:

Functionally graded materials; Heat treatment; Additive manufacturing; CALPHAD

1. Introduction

Functionally graded materials (FGMs) are those in which structure or composition, and therefore, properties vary as a function of position [1]. A key goal of designing composition pathways for FGMs is to achieve better performance compared to direct joining of dissimilar alloys. Direct energy deposition (DED) additive manufacturing (AM) can be used to fabricate components with spatial changes in composition during layer-wise fabrication by delivering different feedstock powders to the melt pool during processing [2]. However, compositional pathways along which to grade between terminal alloys must be designed to avoid cracking [3] and formation of undesired intermetallic phases [4][5]. Additionally, the small melt pool size and repeated thermal cycles during the DED process along with spatially varying compositions lead to residual stresses in the as-deposited samples, resulting in compromised mechanical properties, e.g., a shorter fatigue life [6][7].

Consequently, post-process heat treatments are necessary to reduce residual stresses in the as-built parts prior to use [8]. Determining appropriate heat treatments for FGMs is more challenging than for monolithic components as stress relief settings depend on the temperature-related properties of the alloys and are designed to avoid the formation of harmful phases, both of which vary with composition. Post-processing of FGMs usually consists of heat treating the FGM as a whole part, thus, all compositions in the component should be considered collectively. Furthermore, unlike well-studied terminal alloys in FGMs, the temperature-dependent properties of compositions in FGM gradient regions remain unexplored.

Ni-based superalloy Inconel 625 (IN625) is a high temperature alloy with good creep and

corrosion resistance, thus being widely used in aircrafts, shipbuilding, and power plant industries [9], while grade 304L stainless steel (SS304L) is a widely used structural material that is less expensive than Ni-alloys [10]. The combination of both alloys has potential to be used for low cost corrosion-resistant components, e.g., as the IN625-cladded boiler tubes in nuclear power plants [11]–[13]. Although heat treatments for stainless steel and Inconel have individually been well studied [14]–[17], optimal stress reliefs for these alloys differ from each other, and heat treating components that contain both alloys, and their mixtures, to relieve residual stresses must be studied. As no standards exist for stress relief heat treatment of parts fabricated by the DED process, the heat treatment settings employed in laser powder bed fusion (PBF-LB) are used here as a reference.

PBF-LB company EOS recommends IN625 be stress relieved at 870 ºC for 1 hour and stainless steel 316L (SS316L) at 900 ºC for 2 hours. The longer stress relief time recommended for stainless steel may result in the formation of δ phase and carbides in IN625 [18]. Laves C14, Nb- and Cr-based carbides have been reported in as-deposited DED IN625 [19], and with heat treatments at 800 °C and 900 °C, δ phase has been reported to form, while the γ'' phase has been reported to form at 600 °C and 700 °C in DED IN625 [20]. A high temperature heat treatment (e.g., at or above 1000 °C) can dissolve Laves C14 and δ precipitates in IN625, but it will also result in recrystallization in both IN625 and SS304L, resulting in lower strengths [21]–[23]. A low-temperature heat treatment requires more time to relieve the residual stress, while a long-time low-temperature heat treatment could result in the formation of σ phase in SS304L [24]. In addition to the different temperature-dependent behaviors of the terminal alloys, the phase transformation kinetics in the gradient region from

SS304L to IN625 have yet to be determined. Previous studies on FGMs combining stainless steel and Inconel have revealed the presence of carbides and Laves C14 precipitates in the as-built gradient region [8][25]. The fact that different precipitates exist across the as-deposited FGMs highlights the importance of studying heat treatments of FGMs as full parts.

In the present work, a SS304L to IN625 FGM fabricated by DED AM was subjected to heat treatments at 700 °C, 900 °C, and 1150 °C for 10 hours, 2 hours, and 1 hour, respectively. Compositions and phases along the full FGM were evaluated for as-deposited and heat-treated samples. An approach previously developed by the team, which merges Scheil calculations to consider compositional microsegregation during solidification and equilibrium calculations of microsegregated compositions, termed the hybrid Scheil-equilibrium method [3], was used to predict phases formed in the heat-treated samples. A recently remodeled thermodynamic database considering both Fe- and Ni-rich compositions in ref. [26] was used for the calculations in the present work. The study not only helped to understand the effect of heat treatments on the gradient region of the SS304L to IN625 FGMs but also demonstrated the ability of the newly developed hybrid Scheil-equilibrium method to aid in designing heat treatments for FGMs.

2. Methods

2.1 Experimental methods

A SS304L to IN625 FGM [25] measuring 16 mm × 16 mm × 34 mm was fabricated by DED AM using powders with the compositions shown in **Table 1**. The FGM consisted of 20 layers of SS304L, 24 gradient layers in which the composition of IN625 was increased by 4

volume percent per layer, and 19 layers of IN625. The sample was sectioned into four parts using wire electric discharge machining (see **Figure 1**). The sectioned parts were subjected to low-temperature stress-relief, high-temperature stress-relief, and homogenization heat treatments as described in **Table 2**. All heat treatments used a heating rate of 2.5 °C/min and all samples were water quenched after heat treatment to preserve the phases at the heat treatment temperature. The first heat treatment (HT1) was used to investigate the efficacy of a long-duration, low-temperature heat treatment in preventing the formation of the δ phase. This phase was anticipated to be absent in HT1 based on the time-temperature-transformation (TTT) diagram for the δ phase in IN625 [27]. The second heat treatment (HT2) was a high-temperature stress relief heat treatment performed at the temperature where the fastest kinetics of the δ phase in IN625 was reported [27] to determine the maximum amount of δ phase that would be precipitated in the FGM during such a stress relief. The third heat treatment (HT3) was a homogenization heat treatment used to probe the ability to dissolve precipitates. In all cases, the impact of the heat treatment on the mechanical properties along the FGM was studied through microhardness measurements.

The as-deposited and heat-treated samples were mounted in epoxy resin and prepared for metallurgical examination using standard metallographic grinding and polishing techniques with SiC abrasive disks and a final polish using 0.05 μm alumina suspension. Samples were subsequently electrolytically etched in 10% oxalic acid for 10-15s at 4 V.

Etched samples were imaged using a digital optical microscope (OM) (VHX-2000, Keyence, Japan) to view microstructural features before and after heat treatments. Scanning electron microscope (SEM) imaging and energy dispersive spectroscopy (EDS) (Apreo 2,

ThermoFisher, United States) were performed to assess potential diffusion following heat treatments. Electron backscatter diffraction (EBSD) and X-ray diffraction (XRD) (Empyrean, Malvern Panalytical, United Kingdoms) were used to identify phases present before and after heat treatments. A feritscope (FMP30C, Fischer, Germany) was used to measure the Ferrite Number (FN) at three locations within the SS304L region of each sample [28].

Vickers hardness was measured along the sample height using a 300 gf load and a 15 s dwell time (AMH55 hardness tester, LECO, Germany). For each height, a minimum of five measurements were taken.

2.2 CALPHAD-based calculations

To aid phase identification, equilibrium thermodynamic calculations were made using the CALculation of PHAse Diagrams (CALPHAD) method to predict the amount and composition of each phase at equilibrium as a function of temperature for each given chemistry. High resolution EDS line scans paired with equilibrium calculations were used to aid in the identification of precipitates in heat-treated samples. Thermo-Calc (Thermo-Calc 2016b [29]) was used for all the phase predictions in this study.

To accurately predict phases formed during the DED AM process and subsequent heat treatment of the SS304L to IN625 FGM, a newly developed Cr-Fe-Mo-Nb-Ni thermodynamic database based on the key elements in both SS304L and IN625 was used [26]. This database considers ten binary systems (Cr-Fe, Cr-Mo, Cr-Nb, Cr-Ni, Fe-Mo, Fe-Nb, Fe-Ni, Mo-Nb, Mo-Ni, and Nb-Ni) and ten ternary systems (Cr-Fe-Mo, Cr-Fe-Nb, Cr-Fe-Ni, Cr-

Mo-Nb, Cr-Mo-Ni, Cr-Nb-Ni, Fe-Mo-Nb, Fe-Mo-Ni, Fe-Nb-Ni, and Mo-Nb-Ni). It contains models of 11 topologically close-packed (TCP) phases, also known as the Frank-Kasper phases [30], which are brittle intermetallic compounds having complex crystalline structures and high coordination numbers. These TCP phases are $\delta, \mu, \sigma, \gamma', \gamma''$, Chi, D_NiMo, Laves C14, Laves C15, P, and R as detailed in refs. [30][31]. The selected sublattice models of these TCP phases in this database are based on the Wyckoff positions for each phase, ensuring a more accurate description of phase behavior than reduced sublattice models [32]. For instance, both the μ and σ phases were modelled by a five-sublattice model, while the Laves C14 and δ phases were modelled by a three-sublattice model according to their Wyckoff positions. Additionally, the modelled Nb-Ni binary in this recently developed database exhibits the improved site fraction representation of Nb in the μ phase [33], and the Fe-Nb-Ni ternary represents the latest modeling approach using the full Wyckoff positions in the sublattice models [34]. In addition to validating the database, the ability of the Scheil calculations (ref. [35]) to predict phases formed during AM processing was verified through modeling and experimental investigation of the Cr-Ni-V system [36].

To predict phase transformations during heat treatment by considering solidification microsegregation, hybrid Scheil-equilibrium calculations [3] were performed. In hybrid Scheil-equilibrium calculations, Scheil calculations are first carried out for each composition along the FGM composition path, providing compositions of the liquid and solid phases as a function of the fraction of solid phases, representing information about spatial (i.e., solid fraction-related) distributions of elements. Equilibrium thermodynamic calculations are then performed for each composition of the solid phases to predict phases and their compositions

during subsequent heat treatment.

3. Results and discussion

3.1 Macroscale diffusion and recrystallization during heat treatment

To investigate whether macroscale diffusion occurred during heat treatments in the FGM samples, compositions along the building direction for all the four samples were measured using EDS line scans. The results shown in **Figure 2** indicate that no macroscale diffusion occurred during any of the heat treatments studied herein. As a result, the original FGM compositional path remained after each heat treatment. An exception to this was the fast carbon diffusion occurring along the grain boundaries during recrystallization and grain growth in HT3, which will be discussed in the following section.

Figure 1 shows that the outlines of the melt pools seen in the as-deposited samples remained in samples exposed to HT1 and HT2, while HT3 removed melt pools in the SS304L region. Grain structure in the samples exposed to HT1 and HT2 share high similarity to that in the as-deposited sample while twin boundaries were widely observed in the SS304L sections and SS304L-rich gradient region in the sample exposed to HT3 (see **Figure 3**), indicating recrystallization and following grain growth occurred in this region during HT3. Recrystallization was not observed in IN625 sections or IN625-rich gradient regions in any of the samples, but dendrite structures in the sample exposed to HT3 were removed, indicating homogenization during HT3.

3.2 Phase transformation during heat treatments

SEM imaging was used to investigate phase transformation due to HT1, HT2 and HT3 heat treatments as shown in **Figure 4**. **Figure 4 (a-d)** depicts the ferrite in the SS304L region. While not a quantitative measure of ferrite content, the Ferrite Number measured for the SS304L region was 143±3.79 in the as-deposited, 78.74±7.06 after HT1, 12.2±0.52 after HT2, and 0±0 after HT3, indicating that in the sample exposed to HT1 (700 ºC), the ferrite amount decreased, HT2 (900 ºC) dissolved most of the ferrite and the ferrite completely disappeared after HT3 (1150 ºC). **Figure 4 (e-h)** show the precipitates in the SS304L-rich gradient region. In the as-built sample, Laves C14 particles were found around dendrite intersections and NbC carbides were found along the dendrite boundaries and around Laves C14 particles [8]. In the sample exposed to HT1, the Laves C14 particles grew and were surrounded by carbides. In the sample exposed to HT2, needle-shaped δ phase formed around the Laves C14 phase. HT3 resulted in the dissolution of the Laves C14 phase and a decrease in number but increase in size of carbides.

Figure 4 (i-l) show the precipitates in the IN625 region. In the as-deposited sample, Laves C14 and carbides were found in the interdendritic regions and γ'' phase was found along the dendrite boundaries, matching the phases reported in as-deposited AM IN625 [19]. After HT1, the Laves C14 particles and carbides grew, and small needle-shaped precipitates were found around them.

The XRD pattern obtained in the IN625 region after HT1 is shown in **Figure 5** indicating the presence of the δ phase, suggesting that the needle-shaped precipitates are the δ phase. The observed results differ from the TTT diagram [27], which does not predict the presence of the δ phase after a 10-hour heat treatment at 700 °C. This discrepancy can be attributed to

the difference between PBF-LB fabricated parts, which have been studied in ref. [27], and DED fabricated parts, where microsegregation is different due to a relatively smaller cooling rate in the DED process. Previous studies indicated that the δ phase can form in DED IN625 after heat treatment at 800 ºC for 1 hour, while negligible amounts of the δ phase were found in PBF-LB IN625 after heat treatment at 800 ºC for 1 hour [37][38]. In the sample exposed to HT2, all the γ'' phase disappeared and the needle-shaped δ phase was found around the Laves C14 phase and carbides, which is in alignment with calculations in ref. [18] showing that the γ'' phase is replaced by the δ phase during heat treatments at 800 ºC and 870 ºC. HT3 eliminated all the precipitates in the IN625 region except carbides. While the as-deposited dendritic solidification structure remained throughout the FGM after HT1 and HT2, it was absent after HT3.

Recrystallization was also observed in the SS304L and SS304L-rich gradient region in the sample exposed to HT3, resulting in carbide formation and growth along the grain boundaries during the following grain growth. As shown in **Figure 6 (a)**, the grain boundaries were seen clearly in the SS304L-rich gradient region of the sample exposed to HT3. As shown in **Figure 6 (b)**, EDS maps were collected to identify the precipitates. The increase in Nb and Mo in the precipitates compared to the matrix suggests that these precipitates are Nb- and Mo- carbides. During the grain growth after recrystallization, moving grain boundaries provide fast diffusion pathways for carbide formation [39].

3.3 Scheil calculations for the as-deposited sample

Figure 7 shows the phase fractions from Scheil solidification calculations for the gradient

region, with simplified chemistry of Cr, Fe, Mo, Nb, and Ni, using the recently developed database in ref. [26]. The σ phase is not shown in the plot due to its low amount (<0.005 mole fraction). The Laves C14 phase was predicted to form in the SS304L-rich gradient region, while the δ phase was predicted to form in the IN625-rich gradient region. The predicted amount of BCC phase decreased dramatically at the beginning of the gradient region with increasing IN625 concentration.

However, experimentally, no δ phase was detected in the as-deposited sample. Instead, the Laves C14 was detected in the IN625-rich gradient region and the γ'' phase was detected in the pure IN625 region (**Figure 4 (i-j)**). The difference between the Scheil predictions and experimental results is likely due to the formation of metastable phases; as Scheil calculations assume equilibrium conditions at the solid-liquid interface, the metastable γ'' phase that remains in AM samples due to the high cooling rate is not captured by Scheil calculations. The postulation that this discrepancy is due to metastability is supported by observations after subsequent heat treatments: in the as-deposited sample, γ" phase was detected instead of the δ phase; however, in the sample exposed to HT1, γ" phase was almost entirely replaced by δ phase; after HT2, all the γ" phase disappeared, and the δ phase was detected (as shown in **Figure 4 (i-k)**). The findings indicate that the metastable γ" phase was formed during the fabrication process, and with subsequent heat treatments, the microstructure gradually transitioned towards equilibrium, leading to the replacement of the γ" phase with the δ phase. The δ phase was also observed in the gradient region of the sample exposed to HT2 (see **Figure 4 (g)**), which was supported by hybrid Scheil-equilibrium results as described in the next section. The absence of the δ phase in the gradient region of the sample exposed to HT1

can be due to the slow kinetics of the δ phase at the heat treatment temperature of HT1 (i.e., 700 ºC).

3.4 Hybrid Scheil-equilibrium and equilibrium calculations for samples exposed to HT1 and HT2.

Figure 8 displays the predicted phase fractions from hybrid Scheil-equilibrium and equilibrium calculations after HT1 and HT2, respectively. A notable observation is the divergence between the hybrid Scheil-equilibrium calculations shown in **Figure 8 (a-b)** and the equilibrium calculations shown in **Figure 8 (c-d)**. This discrepancy arises due to the incorporation of solidification microsegregation, specifically interdendritic Nb microsegregation in this sample, in the hybrid Scheil-equilibrium calculations.

In **Figure 7**, the Scheil calculations reveal the prediction of the Laves C14 phase at the SS304L-rich gradient region in the as-deposited sample. In section 3.2, the Laves C14 phase was detected in the gradient region of the samples exposed to HT1 and HT2. However, the equilibrium calculations based on the overall layer composition shown in **Figure 8 (c-d)** do not predict the Laves C14. On the contrary, the hybrid Scheil-equilibrium calculations (**Figure 8 (a-b)**) predict the Laves C14 phase in the gradient region, in agreement with the EBSD data (see **Figure 9**) of the sample exposed to HT2. Additionally, the hybrid calculations predict the formation of the δ phase in the gradient region with a lower IN625 fraction compared to the equilibrium calculations, in agreement with the SEM analysis (see **Figure 4 (g)**). This is because the hybrid Scheil-equilibrium calculations consider the significant Nb microsegregation during the solidification process as shown in the EDS

measurements in **Figure 10**.

Figure 10 plots the composition from the EDS line scan (see **Figure 10 (a)**) and corresponding equilibrium calculation results (see **Figure 10 (b-c)**) for precipitates in the crack region (i.e., SS304L-rich gradient region with ~20-25 wt% IN625) of the sample exposed to HT2. Despite the layer containing only 0.61 wt.% Nb, there exists significant micro-segregation of Nb in the precipitates, which reach as high as 30 wt.%. Equilibrium calculations were carried out for each composition along the EDS line scan using two databases (TCFE8 [40] and the database in ref. [26]). Predicted phase fractions were then plotted in **Figure 10 (b-c)** with the same x-axis with the EDS line scan in **Figure 10 (a)**. Equilibrium calculations for the precipitates here show that these are primarily Laves C14 phase, in agreement with the hybrid Scheil-equilibrium calculations (see **Figure 8 (c)**) and the EBSD map (see **Figure 9**).

The hybrid Scheil-equilibrium calculations offer a rapid estimation of phase transformations during heat treatment without the need for mobility/diffusion data. However, as these rely on equilibrium calculations with composition from Scheil calculations, they do not account for phase transformation kinetics. Consequently, the accuracy of the hybrid Scheil-equilibrium predictions may be compromised in situations where the phase formation kinetics are slow or when the heat treatment duration is short. For instance, the δ phase predicted in the gradient region of the sample exposed to HT1 (see **Figure 8 (a)**) was not observed in SEM imaging (see **Figure 4 (f)**) due to the slow kinetics of the δ phase formation at 700 °C for these compositions. Similar discrepancies may arise for the Chi, P, and σ phases. Another limitation of the hybrid Scheil-equilibrium calculations is that they ignore diffusion

during heat treatment. Diffusion of substitutional elements during these stress-relief heat treatments is typically slow, but for interstitial elements such as carbon, diffusion is not negligible, resulting in difference between predictions and experiments. Nevertheless, as previously discussed, the hybrid Scheil-equilibrium calculations provide superior prediction of phases formed in comparison with Scheil calculations or equilibrium predictions alone, offering a rapid assessment of phases in AM and providing a route for high throughput calculations for the design of FGM gradient pathways [3].

3.5 Hardness as a function of position and heat treatment

To investigate how the heat treatments impacted mechanical properties along the FGM, Vickers microhardness measurements were taken along as-deposited and heat-treated samples, with results shown in **Figure 11**. Hardness is influenced by features including residual stress, dislocation density, precipitates, and grain size. Grain growth was negligible in samples exposed to HT1 and HT2, while the grain size in the sample exposed to HT3 was smaller than as-deposited due to recrystallization. However, despite a smaller grain size, the hardness of the sample exposed to HT3 was less than the as-deposited sample, indicating that the decrease in residual stress/dislocation density and dissolution of precipitates played a more significant role in the change in hardness. Compared to the as-deposited condition, dramatic increase in hardness in the IN625-rich gradient region and the IN625 region was observed after HT1. The hardness increase in the IN625 region is likely a result of carbide growth and δ phase formation (see **Figure 4 (i-j)** and **Figure 5**). Compared to the hardness in the as-deposited sample, the hardness decreased in the SS304L region following HT2. According to

Figure 4 (c) and feritscope measurements, the ferrite phase was almost completely removed in the SS304L region following HT2, resulting in a decrease in hardness in that region. In the gradient and IN625 regions, there was a competition between the decrease in hardness due to residual stress relief and the increase in hardness from precipitation (as shown in **Figure 4 (j)(k)**), resulting in a minimal change in hardness after HT2. HT3 resulted in a significant decrease in hardness along the FGM compared to its as-deposited condition due to recrystallization in the SS304L and SS304L-rich gradient regions (see **Figure 3**), dissolution of dendritic structures and precipitates (with the exception of some carbides) in the gradient and IN625 regions (as depicted in **Figure 4 (h)(l)**), and the relief of residual stress throughout the entire sample.

4. Conclusions

In the present work, the impact of three heat treatments on the microstructure and mechanical properties of an SS304L to IN625 FGM were examined. The evolution of microstructural features due to the three heat treatments were characterized using OM, SEM, EDS, XRD, and EBSD, and thermodynamic calculations were conducted to aid in the phase identification. The capability of hybrid Scheil-equilibrium calculations to predict phases in as-built and heat-treated samples was demonstrated.

Among the three heat treatments carried out in this study, HT2 was optimal, as HT1 resulted in a significant hardness increase in the IN625 region, and HT3 caused excessive softening along the FGM. The hybrid Scheil-equilibrium predictions were found to be closer to experimental results because it considered solidification microsegregation, validating its

capability of helping with FGM path and heat treatment design. In addition to the SS304L to IN625 alloy system investigated in this study, the hybrid Scheil-equilibrium calculations can also be applied to other material systems, offering a rapid and straightforward prediction of phase formation at various temperatures considering solidification microsegregation, aiding in determining heat treatment temperatures for desired phases.

The key findings of this study were as follows:

- A heat treatment at 700 ºC for 10 hours (HT1) resulted in carbide growth in both the gradient region and the IN625 region, as well as the formation of the δ phase in the IN625 region, thus the increase in hardness in both regions.
- A heat treatment at 900 ºC for 2 hours (HT2) dissolved the ferrite phase in the SS304L region, resulting in a hardness decrease in the SS304L region. Additionally, the formation of the δ phase was observed in both the gradient region and the IN625 region, with a higher amount in the IN625 region, indicating the faster kinetics in the IN625 region. The competition between the hardness increase due to the δ phase formation and the hardness decrease due to the stress relief resulted in an unchanged hardness in the gradient and the IN625 region in the sample exposed to HT2.
- A heat treatment at 1150 ºC for 1 hour (HT3) resulted in recrystallization and grain growth of the recrystallized grains in the SS304L region and the SS304L-rich gradient region and removed the dendrite structure and most precipitates in the gradient and the IN625 region, resulting in a dramatic decrease in hardness along the entire FGM. Carbides formed along grain boundaries at the SS304L-rich side of the FGM.

- Hybrid Scheil-equilibrium calculations were conducted at temperatures of 700 ºC and 900 ºC along the SS304L to IN625 FGM. In comparison with the equilibrium calculations using the layer composition, the hybrid Scheil-equilibrium calculations accurately predicted the experimentally observed Laves C14 phase in the heat-treated sample. While the phases predicted by the Scheil-equilibrium calculations did not match experimental results for phases with slow phase transformation kinetics (e.g., TCP phases of Chi and P) or for short duration heat treatments. This efficient prediction method does not require a mobility/diffusion database. In contrast to equilibrium calculations, this method offers a direct and convenient means to estimate heat treatment outcomes while accounting for solidification microsegregation.

5. Acknowledgments

The authors are grateful for financial support from the National Science Foundation (NSF Grant CMMI-2050069) and the Office of Naval Research (ONR Grant N00014-21-1-2608).

Declaration of competing interests:

None

Data availability:

All relevant data are available from the authors.

References

[1] A. Reichardt *et al.*, "Advances in additive manufacturing of metal-based functionally graded materials," *Int. Mater. Rev.*, vol. 66, no. 1, pp. 1–29, 2021, doi: 10.1080/09506608.2019.1709354.

[2] T. DebRoy *et al.*, "Additive manufacturing of metallic components – Process, structure and properties," *Prog. Mater. Sci.*, vol. 92, pp. 112–224, 2018, doi: 10.1016/j.pmatsci.2017.10.001.

[3] Z. Yang, H. Sun, Z. K. Liu, and A. M. Beese, "Design methodology for functionally graded materials: Framework for considering cracking," *Additive Manufacturing*, vol. 73. 2023. doi: 10.1016/j.addma.2023.103672.

[4] B. Bocklund, L. D. Bobbio, R. A. Otis, A. M. Beese, and Z. K. Liu, "Experimental validation of Scheil–Gulliver simulations for gradient path planning in additively manufactured functionally graded materials," *Materialia*, vol. 11, no. April, 2020, doi: 10.1016/j.mtla.2020.100689.

[5] L. D. Bobbio *et al.*, "Design of an additively manufactured functionally graded material of 316 stainless steel and Ti-6Al-4V with Ni-20Cr, Cr, and V intermediate compositions," *Addit. Manuf.*, vol. 51, no. February, p. 102649, 2022, doi: 10.1016/j.addma.2022.102649.

[6] C. Li, Z. Y. Liu, X. Y. Fang, and Y. B. Guo, "Residual Stress in Metal Additive Manufacturing," *Procedia CIRP*, vol. 71, pp. 348–353, 2018, doi: 10.1016/j.procir.2018.05.039.

[7] K. Carpenter and A. Tabei, "On residual stress development, prevention, and

compensation in metal additive manufacturing," *Materials (Basel).*, vol. 13, no. 2, 2020, doi: 10.3390/ma13020255.

[8] T. Li, Z. Wang, S. Hu, Z. Yang, and Y. Wang, "Hot cracking during the fabrication of Inconel 625/stainless steel 308 L functionally graded material by dual-wire arc additive manufacturing," *J. Manuf. Process.*, vol. 82, no. August, pp. 461–473, 2022, doi: 10.1016/j.jmapro.2022.08.018.

[9] K. Lyczkowska and J. Michalska, "Studies on the Corrosion Resistance of Laser-Welded Inconel 600 and Inconel 625 Nickel-Based Superalloys," *Arch. Metall. Mater.*, vol. 62, no. 2, pp. 653–656, 2017, doi: 10.1515/amm-2017-0100.

[10] G. Gedge, "Structural uses of stainless steel - buildings and civil engineering," *J. Constr. Steel Res.*, vol. 64, no. 11, pp. 1194–1198, 2008, doi: 10.1016/j.jcsr.2008.05.006.

[11] T. E. Abioye, D. G. McCartney, and A. T. Clare, "Laser cladding of Inconel 625 wire for corrosion protection," *J. Mater. Process. Technol.*, vol. 217, pp. 232–240, 2015, doi: 10.1016/j.jmatprotec.2014.10.024.

[12] M. Shakil *et al.*, "Microstructure and hardness studies of electron beam welded Inconel 625 and stainless steel 304L," *Vacuum*, vol. 110, pp. 121–126, 2014, doi: 10.1016/j.vacuum.2014.08.016.

[13] J. B. Morake, J. M. Mutua, M. M. Ruthandi, and E. O. Olakanmi, "The potential use of laser cladded functionally graded materials to mitigate degradation in boiler tube heat exchangers for power plant applications: a review," *Surf. Eng.*, 2023, doi: 10.1080/02670844.2023.2249653.

[14] X. Zhang *et al.*, "Evolution of Microstructure, Residual Stress, and Tensile Properties of Additively Manufactured Stainless Steel Under Heat Treatments," *JOM*, vol. 72, no. 12, pp. 4167–4177, Dec. 2020, doi: 10.1007/s11837-020-04433-9.

[15] F. Zhang *et al.*, "Effect of heat treatment on the microstructural evolution of a nickel-based superalloy additive-manufactured by laser powder bed fusion," *Acta Mater.*, vol. 152, pp. 200–214, Jun. 2018, doi: 10.1016/j.actamat.2018.03.017.

[16] J. T. Pacheco *et al.*, "Laser directed energy deposition of AISI 316L stainless steel: The effect of build direction on mechanical properties in as-built and heat-treated conditions," *Adv. Ind. Manuf. Eng.*, vol. 4, no. November 2021, p. 100079, 2022, doi: 10.1016/j.aime.2022.100079.

[17] S. Qin, T. C. Novak, M. K. Vailhe, Z. K. Liu, and A. M. Beese, "Plasticity and fracture behavior of Inconel 625 manufactured by laser powder bed fusion: Comparison between as-built and stress relieved conditions," *Mater. Sci. Eng. A*, vol. 806, Mar. 2021, doi: 10.1016/j.msea.2021.140808.

[18] G. Lindwall *et al.*, "Simulation of TTT Curves for Additively Manufactured Inconel 625," *Metall. Mater. Trans. A Phys. Metall. Mater. Sci.*, vol. 50, no. 1, pp. 457–467, Jan. 2019, doi: 10.1007/s11661-018-4959-7.

[19] B. Dubiel and J. Sieniawski, "Precipitates in additively manufactured inconel 625 superalloy," *Materials (Basel).*, vol. 12, no. 7, 2019, doi: 10.3390/ma12071144.

[20] G. Marchese *et al.*, "INCONEL 625 BY DIRECT METAL LASER SINTERING: EFFECTS OF THE PROCESS PARAMETERS AND HEAT TREATMENTS ON MICROSTRUCTURE AND HARDNESS."

[21] P. Petrzak, K. Kowalski, and M. Blicharski, "Analysis of phase transformations in Inconel 625 alloy during annealing," *Acta Phys. Pol. A*, vol. 130, no. 4, pp. 1041–1044, 2016, doi: 10.12693/APhysPolA.130.1041.

[22] Y. L. Hu, Y. L. Li, S. Y. Zhang, X. Lin, Z. H. Wang, and W. D. Huang, "Effect of solution temperature on static recrystallization and ductility of Inconel 625 superalloy fabricated by directed energy deposition," *Mater. Sci. Eng. A*, vol. 772, Jan. 2020, doi: 10.1016/j.msea.2019.138711.

[23] M. Ghayoor, K. Lee, Y. He, C.-H. Chang, B. K. Paul, and S. Pasebani, "Selective Laser Melting of 304L Stainless Steel: Role of Volumetric Energy Density on the Microstructure, Texture and Mechanical Properties."

[24] C.-C. Hsieh and W. Wu, "Overview of Intermetallic Sigma () Phase Precipitation in Stainless Steels," *ISRN Metall.*, vol. 2012, pp. 1–16, Mar. 2012, doi: 10.5402/2012/732471.

[25] B. E. Carroll *et al.*, "Functionally graded material of 304L stainless steel and inconel 625 fabricated by directed energy deposition: Characterization and thermodynamic modeling," *Acta Mater.*, vol. 108, pp. 46–54, Apr. 2016, doi: 10.1016/j.actamat.2016.02.019.

[26] H. Sun, "Thermodynamic database for Cr-Fe-Mo-Nb-Ni." Zenodo, Jan. 2024. doi: 10.5281/zenodo.10568692.

[27] M. R. Stoudt *et al.*, "The Influence of Annealing Temperature and Time on the Formation of δ-Phase in Additively-Manufactured Inconel 625," *Metall. Mater. Trans. A*, vol. 49, no. 7, pp. 3028–3037, Jul. 2018, doi: 10.1007/s11661-018-4643-y.

[28] "Welding — Determination of Ferrite Number (FN) in austenitic and duplex ferritic-austenitic Cr-Ni stainless steel weld metals." ISO Standard 8249:2018. [Online]. Available: https://www.iso.org/obp/ui/en/#iso:std:iso:8249:ed-3:v1:en

[29] J. O. Andersson, T. Helander, L. Höglund, P. Shi, and B. Sundman, "Thermo-Calc & DICTRA, computational tools for materials science," *Calphad Comput. Coupling Phase Diagrams Thermochem.*, vol. 26, no. 2, pp. 273–312, 2002, doi: 10.1016/S0364-5916(02)00037-8.

[30] F. C. Frank and J. S. Kasper, "Complex alloy structures regarded as sphere packings. I. Definitions and basic principles," *Acta Crystallogr.*, vol. 11, no. 3, pp. 184–190, 1958, doi: 10.1107/s0365110x58000487.

[31] B. Seiser, R. Drautz, and D. G. Pettifor, "TCP phase predictions in Ni-based superalloys: Structure maps revisited," *Acta Mater.*, vol. 59, no. 2, pp. 749–763, 2011, doi: 10.1016/j.actamat.2010.10.013.

[32] I. Ansara *et al.*, "Group 2: Alloy System I - Thermodynamic Modelling of Selected Topologically Close-Packed Intermetallic Compounds," *Calphad Comput. Coupling Phase Diagrams Thermochem.*, vol. 21, no. 2, pp. 171–193, 1997.

[33] H. Sun, S. L. Shang, R. Gong, B. J. Bocklund, A. M. Beese, and Z. K. Liu, "Thermodynamic modeling of the Nb-Ni system with uncertainty quantification using PyCalphad and ESPEI," *Calphad Comput. Coupling Phase Diagrams Thermochem.*, vol. 82, no. March, p. 102563, 2023, doi: 10.1016/j.calphad.2023.102563.

[34] H. Sun, C. Wang, S. L. Shang, A. M. Beese, J. C. Zhao, and Z. K. Liu, "Thermodynamic modeling of Fe-Nb and Fe-Nb-Ni systems supported by first-

principles calculations and diffusion-multiple measurements," *Acta Mater.*, vol. 268, no. February, p. 119747, 2024, doi: 10.1016/j.actamat.2024.119747.

[35] E. Scheil, "Bemerkungen zur Schichtkristallbildung," *Int. J. Mater. Res.*, vol. 34, no. 3, pp. 70–72, 1942, doi: doi:10.1515/ijmr-1942-340303.

[36] B. Tonyali *et al.*, "Additively manufactured Ni-20Cr to V functionally graded material: computational predictions and experimental verification of phase formations," *J. Alloys Compd.*, 2024, doi: 10.1016/j.jallcom.2024.174011.

[37] G. P. Dinda, A. K. Dasgupta, and J. Mazumder, "Laser aided direct metal deposition of Inconel 625 superalloy: Microstructural evolution and thermal stability," *Mater. Sci. Eng. A*, vol. 509, no. 1–2, pp. 98–104, 2009, doi: 10.1016/j.msea.2009.01.009.

[38] E. A. Lass *et al.*, "Formation of the Ni3Nb δ-Phase in Stress-Relieved Inconel 625 Produced via Laser Powder-Bed Fusion Additive Manufacturing," *Metall. Mater. Trans. A Phys. Metall. Mater. Sci.*, vol. 48, no. 11, pp. 5547–5558, Nov. 2017, doi: 10.1007/s11661-017-4304-6.

[39] B. R. A.R.JONES, "The Influence of recrystallization on carbide particle distributions in a fully stabilized austenitic steel," *ACTA Metall.*, vol. 23, 1975.

[40] "Thermo-calc 2015b." https://thermocalc.com/blog/thermo-calc-2015a-release/

Figures

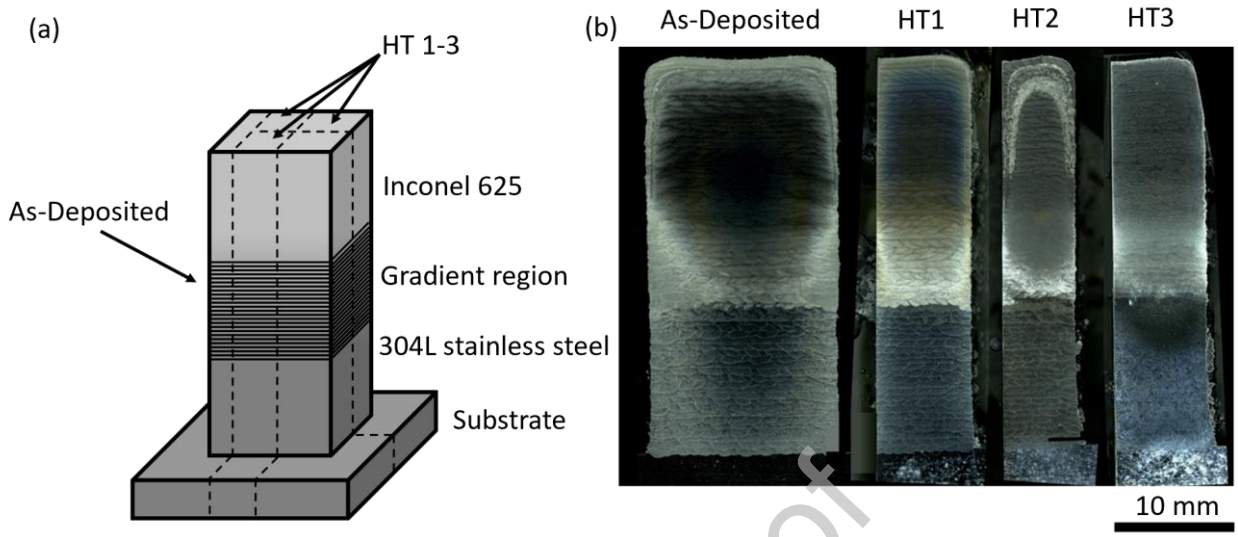

Figure 1: (a) Schematic of the SS304L to IN625 FGM, where dotted lines show how the part was sectioned for heat treatment and analysis. (b) OM images of etched as-deposited and heat-treated samples.

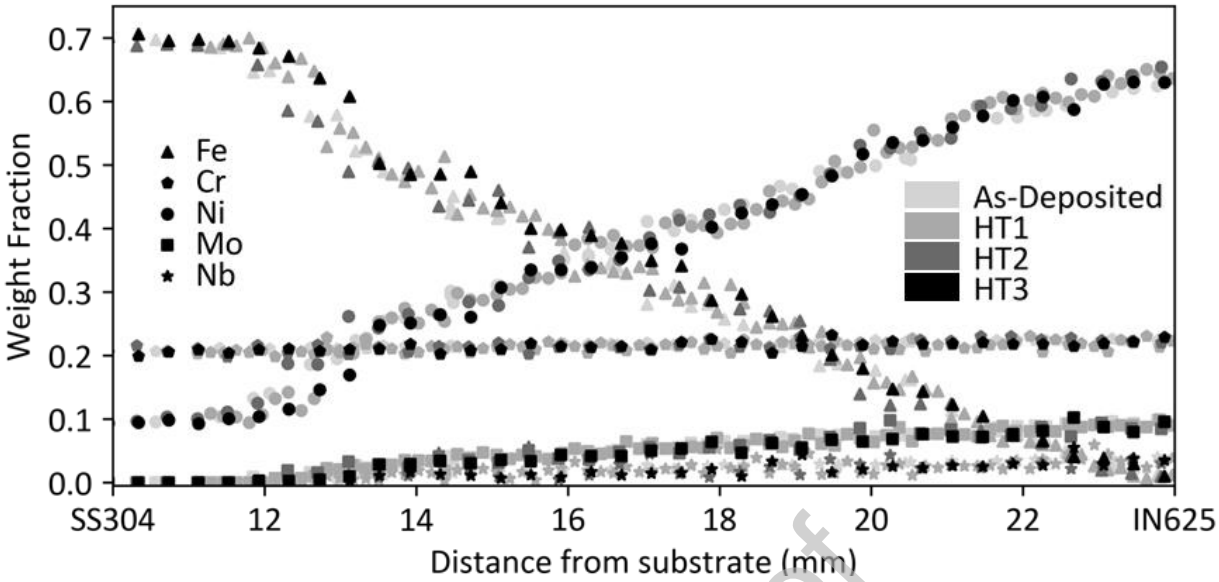

Figure 2: Weight fraction of elements as a function of distance from substrate from EDS line scans along the height of the SS304L to IN625 FGM in as-deposited and heat-treated conditions, where grayscales indicate different samples, and the symbols indicate different elements.

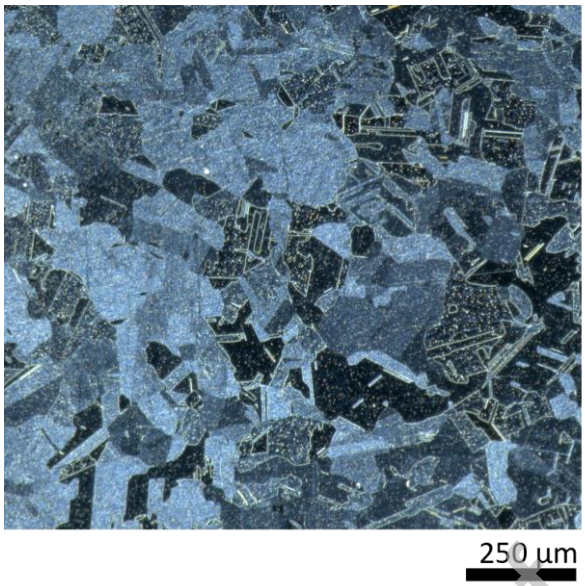

Figure 3: OM image of the SS304L region in the HT3 sample where the presence of twin boundaries indicates recrystallization during the heat treatment.

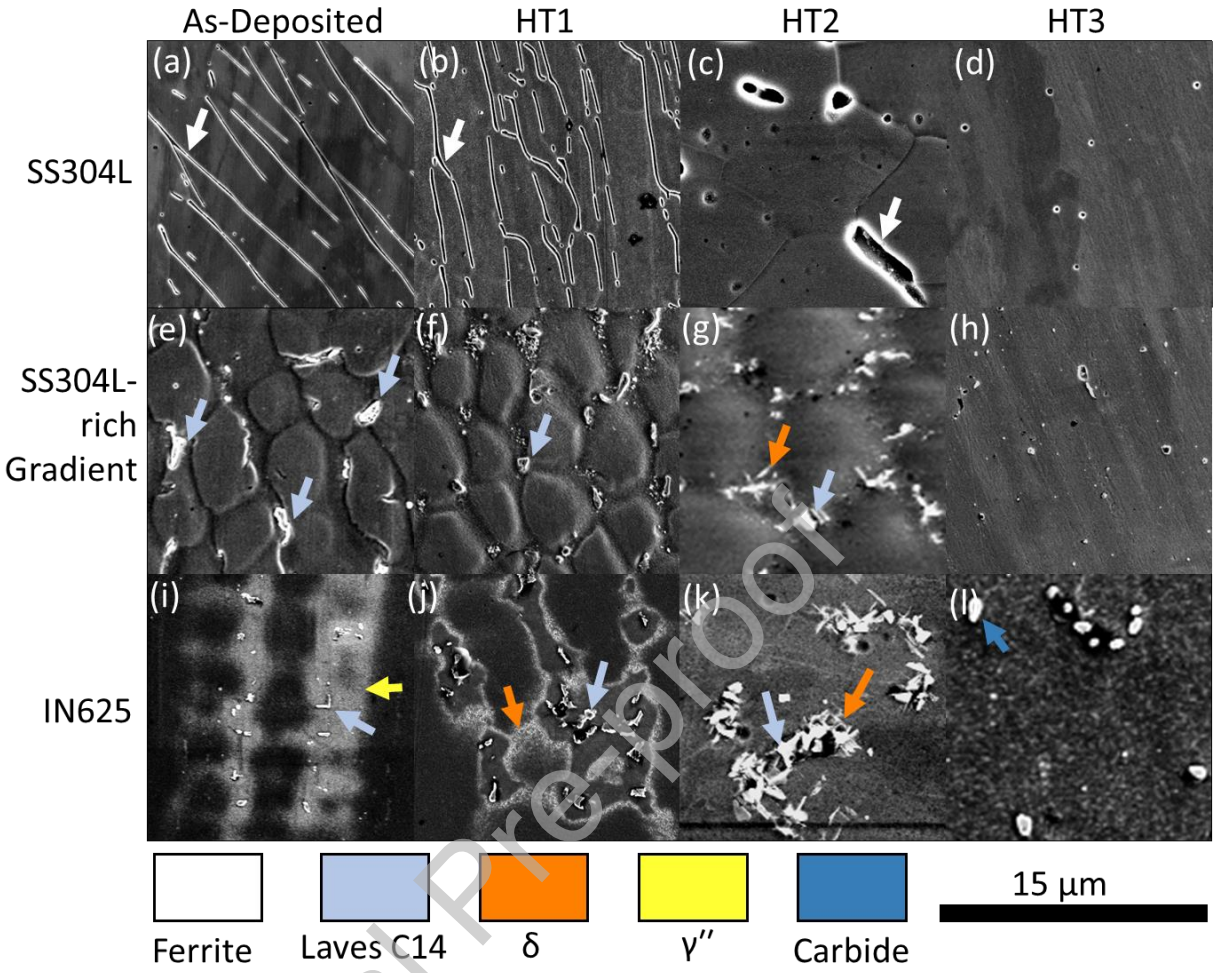

Figure 4: SEM images of the etched SS304L to IN625 FGM samples, with columns corresponding to heat treatment and rows corresponding to position in the samples. (a-d) Show ferrite phase in the SS304L region; (e-h) show Laves C14 phase in the gradient region (~ 80 wt.% SS304L / 20 wt.% IN625); (i-l) show γ'', δ, Laves C14 and NbC phases in the IN625 region. Arrows in the images show the corresponding phases.

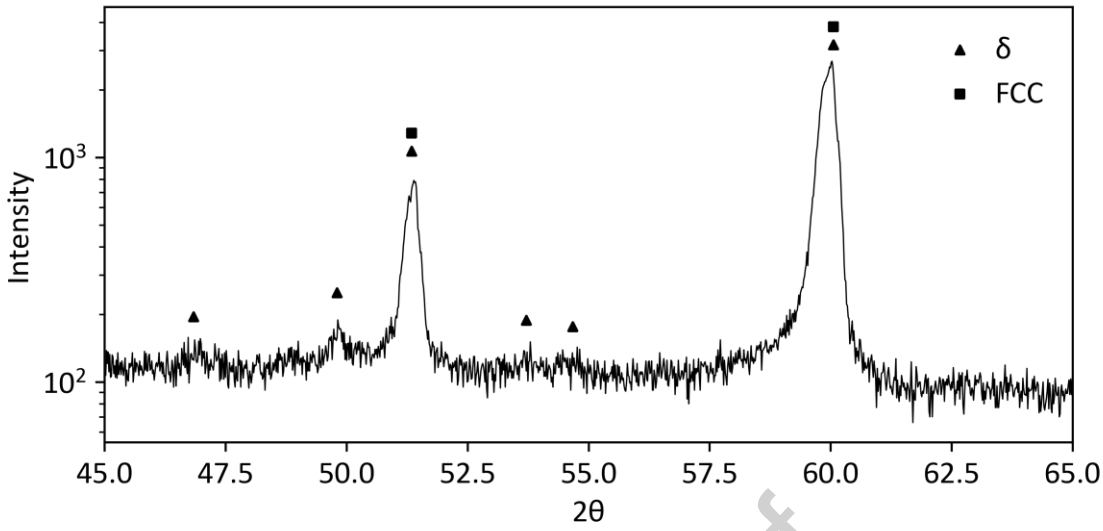

Figure 5: XRD pattern for the IN625 region of the sample exposed to HT1 showing the existence of the δ phase.

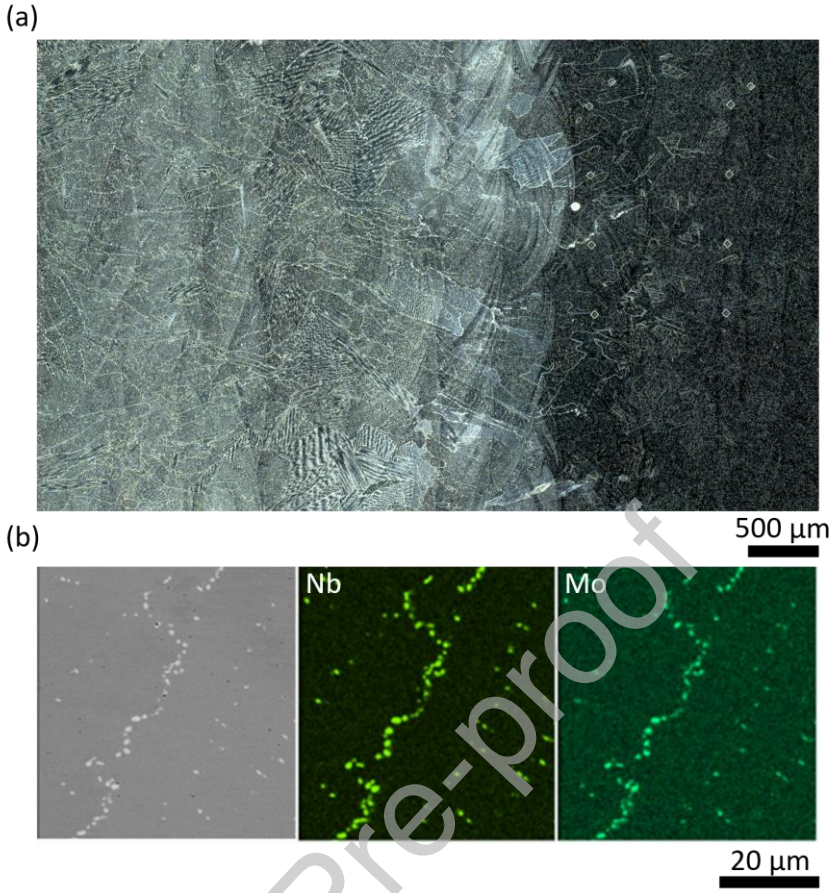

Figure 6: Images show that recrystallization in the SS304L region and the SS304L-rich gradient region in the sample exposed to HT3 also results in carbides forming and growing along the new grain boundaries. (a) OM image shows the grain boundaries in the SS304L-rich gradient region after HT3, where the right side is SS304L region, and the left side is the SS304L-rich gradient region. (b) SEM image, EDS Nb map, and EDS Mo map show Nb- and Mo-rich precipitates along the grain boundaries after HT3.

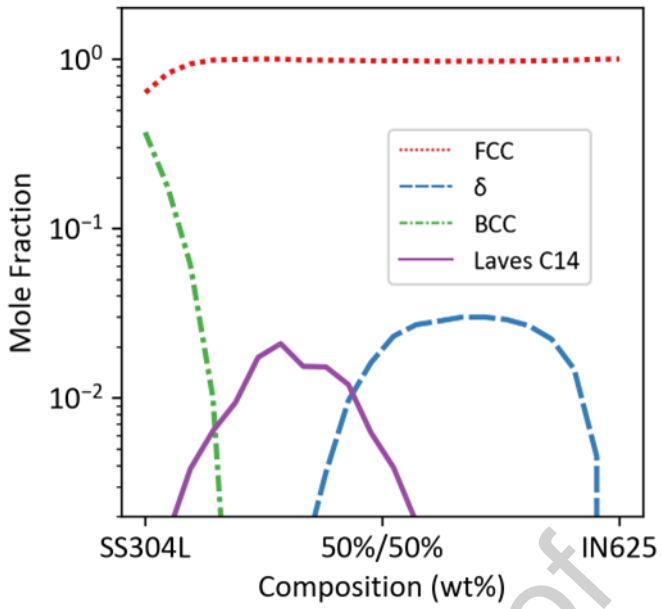

Figure 7: Mole fractions of phases in the gradient region of the SS304L to IN625 FGM predicted by Scheil calculations using the database in ref. [26]. Compositions used in the Scheil calculations were simplified to Cr, Fe, Mo, Nb, and Ni.

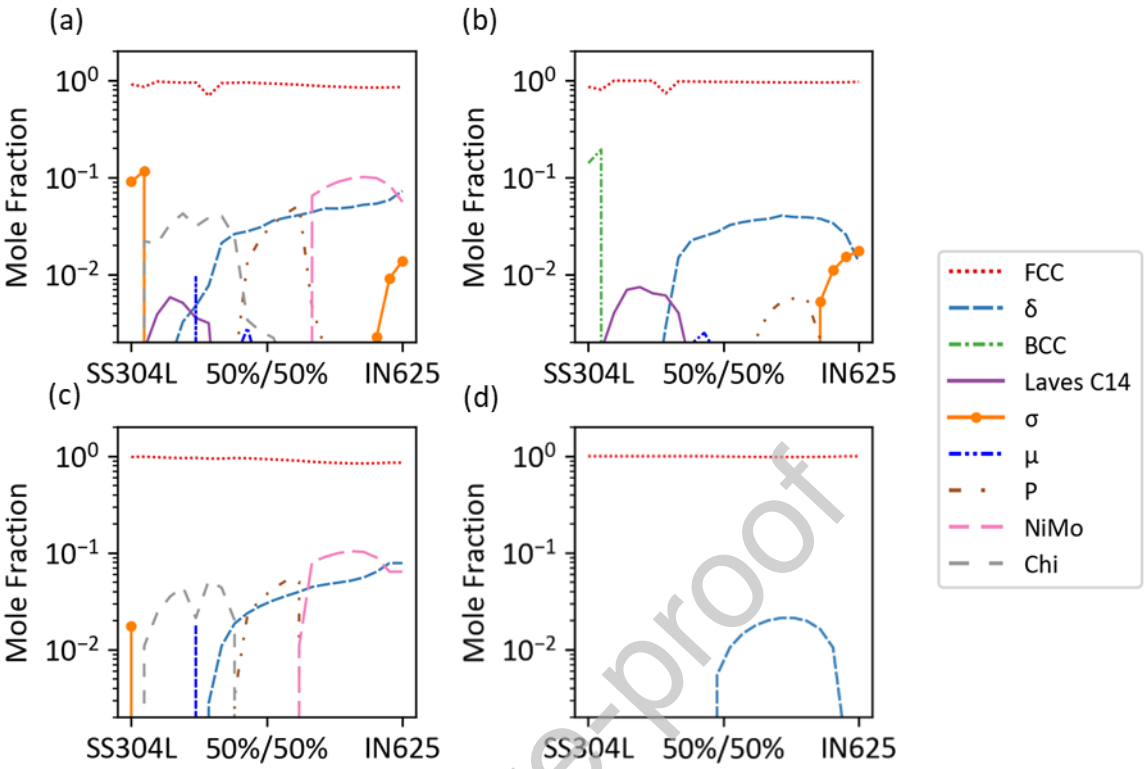

Figure 8: Mole fractions of phases from hybrid Scheil-equilibrium and equilibrium calculations for the heat-treated FGM samples using the database in ref. [26]. (a-b) Hybrid Scheil-equilibrium calculations, where (a) corresponds to heat treatment at 700 ºC and (b) corresponds to heat treatment at 900 ºC. (c-d) Equilibrium calculations usings layer compositions (c) for the 700 ºC heat treatment and (d) for the 900 ºC heat treatment.

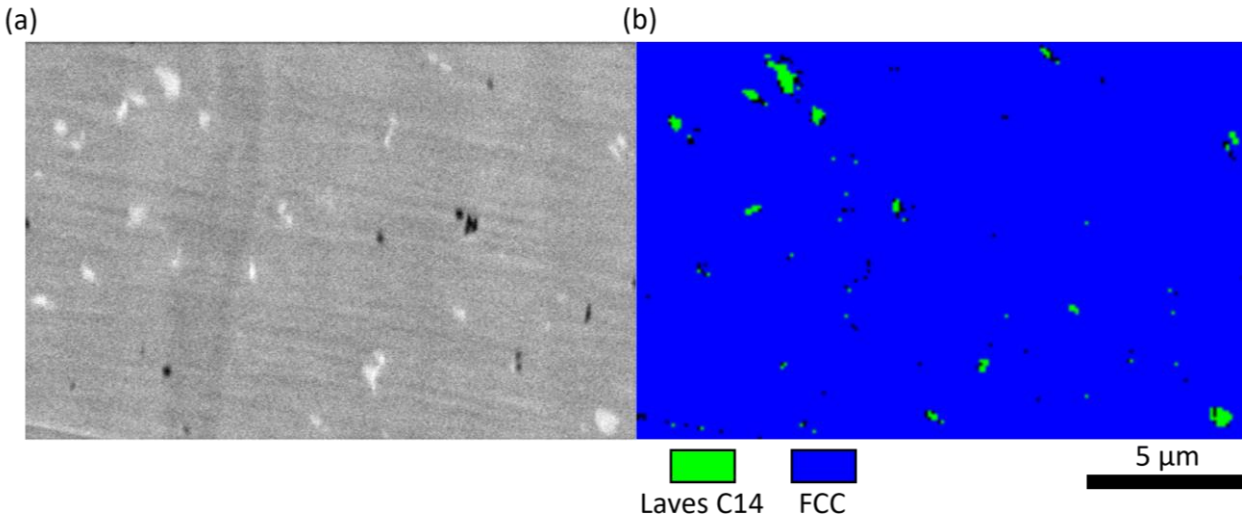

Figure 9: (a) Forescatter detector SEM image showing the Z contrast image of the SS304L-rich gradient region in the sample exposed to HT2. (b) EBSD phase map showing that the precipitates here are Laves C14 phase.

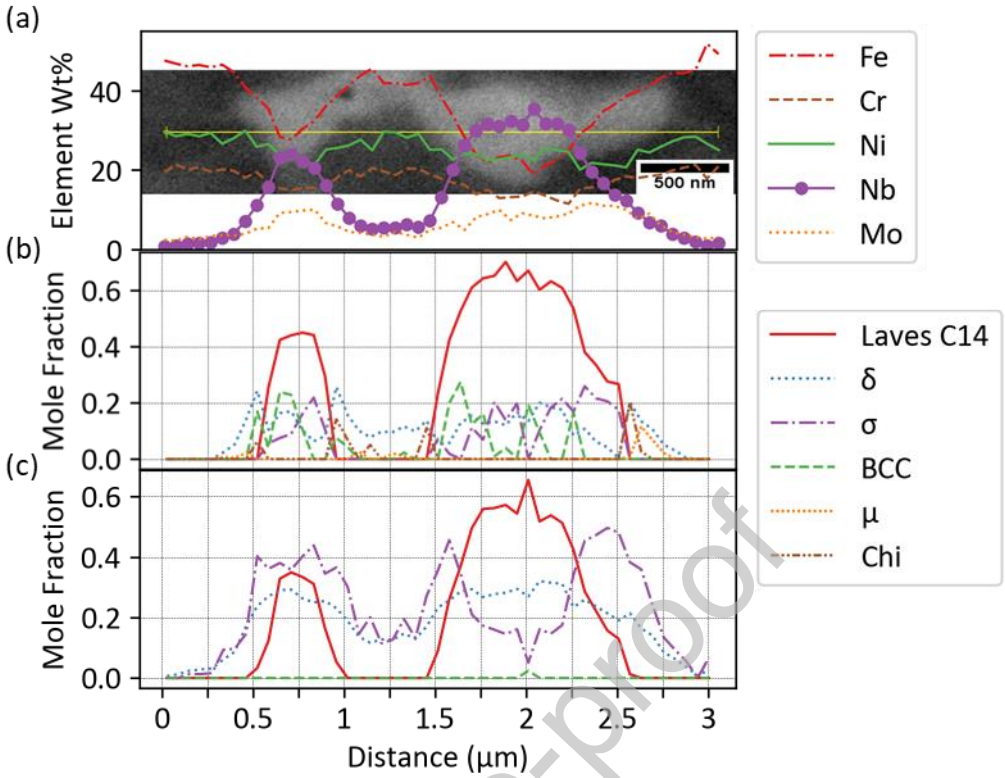

Figure 10: Mole fractions of elements from the EDS line scan for precipitate at the crack region of the sample exposed to HT2 and equilibrium calculations for the EDS result using the database in ref. [26] and TCFE8 [40] . (a) Composition along the EDS line scan overlaying the back-scattered electron image, (b) equilibrium calculations at 900 ℃ using the database in ref. [26] (FCC phase is not shown here) and (c) equilibrium calculations at 900 ℃ using TCFE8 (FCC phase is not shown here).

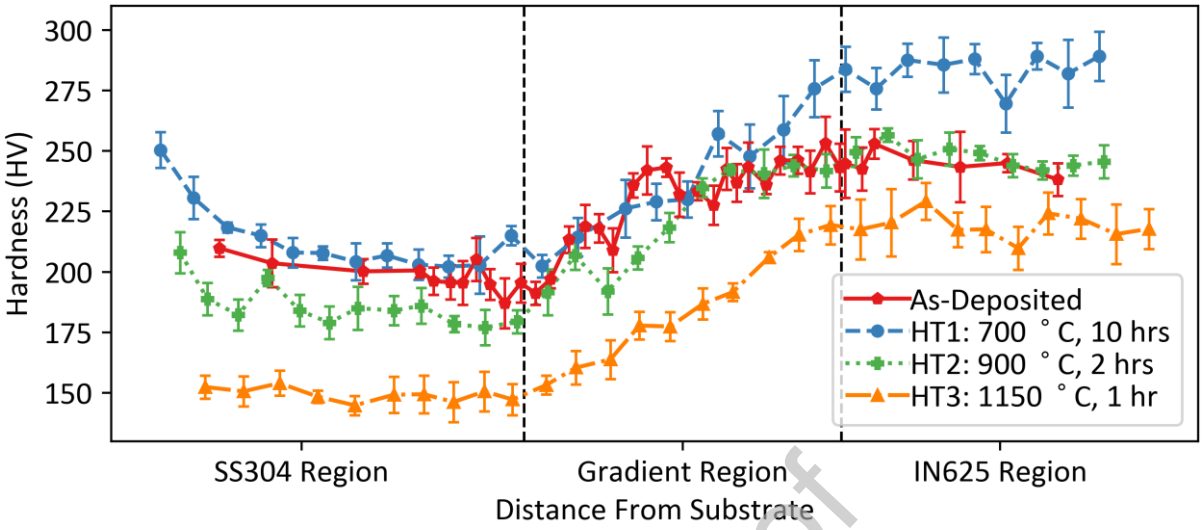

Figure 11: Vickers hardness as a function of position in the SS304L to IN625 FGM before and after heat treatments.

Tables

Table 1 Composition of powders for the terminal alloys in weight percent.

	IN625	SS304L
Ni	65.7	9.4
Fe	<0.1	68.9
Cr	21	19.5
Mo	8.7	-
Nb	3.4	-
Mn	0.36	1.31
Si	0.36	0.66
Co	0.3	-
Ti	0.07	-
Al	0.09	-
C	<0.01	0.017

Table 2: Settings and expected results for the heat treatments in this study.

Heat up (℃/min)	**Temperature (℃)**	**Time (hr)**	**Purpose**
2.5	700	10	Low temperature to avoid formation of the δ phase in IN625 regions, long time to relieve residual stresses
2.5	900	2	Recommended HT parameter by EOS for PBF-LB SS316 parts
2.5	1150	1	Homogeneous HT to dissolve all the δ phase and recrystallize SS304

Graphical abstract

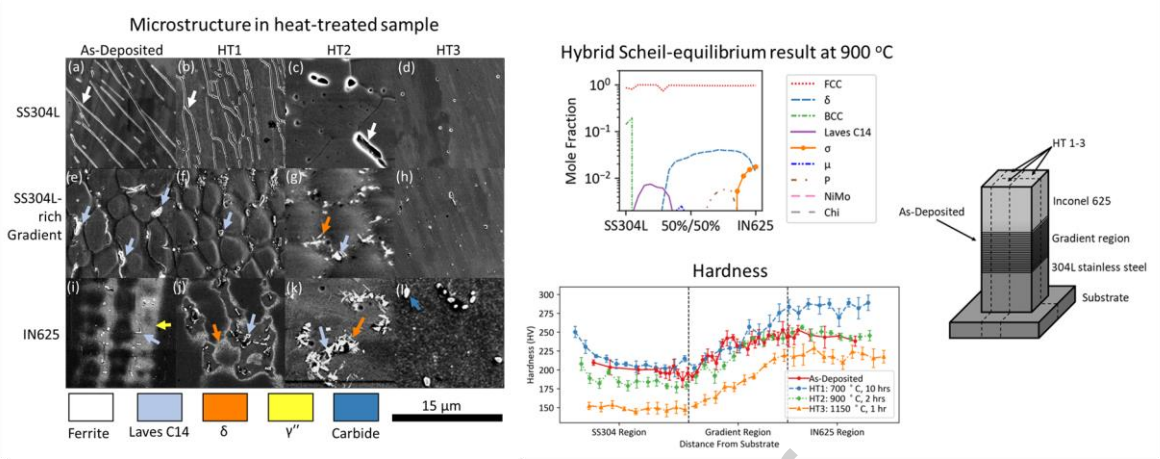

Declaration of interests

☒ The authors declare that they have no known competing financial interests or personal relationships that could have appeared to influence the work reported in this paper.

☐ The authors declare the following financial interests/personal relationships which may be considered as potential competing interests: